Optics & Laser Technology 189 (2025) 113119

Contents lists available at ScienceDirect

Optics and Laser Technology

journal homepage: www.elsevier.com/locate/optlastec

The effect of process parameters on the high-speed cut quality of Li-ion electrodes using a single mode continuous fiber laser☆

Caterina Angeloni *, Carolina Magrini, Erica Liverani, Alessandro Fortunato

Department of Industrial Engineering (DIN), Alma Mater Studiorum – University of Bologna, viale Risorgimento 2, Bologna, Italy

ARTICLE INFO

Keywords:
Laser cutting
Continuousfiber laser
Battery electrodes
Graphite anode
Lithium iron phosphate
High quality
High speed

ABSTRACT

Coated Al and Cu current collectors are employed in the production of Li-ion batteries (LIBs) serving as cathodes and anodes, respectively. The increasing demand and the need for net zero-defect cutting quality are driving industrial production towards fast and reliable technologies. Laser cutting of LIB electrodes is an efficient and cost-effective alternative to conventional mechanical methods, enabling high accuracy and less damaged active material while maintaining high processing speeds. Thanks to remote laser technology flexibility, several combinations of process parameters, electrode material, and thicknesses of the electrode sandwich have been studied. This material variety discussed in the literature reflects the need of the industry to exploit different solutions. Currently, electrode cutting mainly involves the application of short pulse nanosecond (ns) fiber laser. However, the fast-advancing technology of laser manufacturing (including laser sources, optics and scanning heads) allows for new opportunities to improve process productivity and quality. This study evaluates the interaction between a single mode (SM) continuous wave (CW) source and LIB electrodes, exploring the effects of laser power and scanning speed (up to 11 m/s) on thermal defects. These include clearance width and heat affected zone (HAZ) for the anode, as well as HAZ width and the quantity of spherical defects detached from the aluminum foil for the cathode. This investigation identified a significant reduction of defects for both materials when higher speeds are set. Specifically, high-quality cuts were achieved at 5.5 m/s for the anode and 4.4 m/s for the cathode, with a clearance width kept below 20 μm and HAZ under 30 μm.

1. Introduction

Lithium-ion batteries (LIBs) are secondary rechargeable batteries representing a highly widespread technology implemented in hybrid electric vehicles, electronic devices, energy storage and home appliances [1]. The increasing demand for LIBs is attributed to a high energy density, low self-discharge and good energy to weight ratio[2,3]. The manufacturing of LIBs is mainly divided into three steps: electrode production, cell assembly and electrochemical deposition for safe battery usage[4], where an efficient preparation of electrodes can ensure less material waste and lower costs of the production line. In other words, the production of LIBs electrodes should aim to net-zero defects.

The fast-advancing technology of laser material processing (LMP) is an efficient, flexible, contact-free process that is implemented in the electrode manufacturing industry for several steps, including drying of active materials, cutting of electrodes and welding [5–8]. In fact, LMP exhibits several advantages in comparison to mechanical processing. This is because it is a wear-free process with low thermal impact, leading to a small heat affected zone (HAZ) as well as reducing the energy cost and increasing production speed [2,7–9].

In recent years, the scientific community has driven its attention towards finding optimal laser parameters to obtain electrode cutting of high quality[10]. However, the sandwich-like structure of electrodes makes LMP challenging. Specifically, the anode is made of Cu-foil with a layer of graphite on both sides, while the cathode is made of Al-foil sandwiched between two layers of active material, which can include $LiCoO_2$, lithium nickel manganese cobalt (NMC) or $LiFePO_4$ (LFP). The state-of-the-art for the ideal parameter window mostly focuses on applying short pulse nanosecond fiber laser and subsequently analyse the effect of laser parameters on kerf geometry, defect formation and HAZ size. Nanosecond pulsed lasers can achieve high beam qualities and reduce HAZ size thanks to the low thermal contribution at high processing speeds. The short interaction time can prevent the conduction of heat across the material with a discontinuous energy input [11]

☆ This article is part of a special issue entitled: 'LaserEMobility' published in Optics and Laser Technology.

* Corresponding author.
E-mail address: caterina.angeloni2@unibo.it (C. Angeloni).

https://doi.org/10.1016/j.optlastec.2025.113119
Received 17 January 2025; Received in revised form 4 April 2025; Accepted 20 April 2025
Available online 9 May 2025

maintaining high velocity, which made nanosecond lasers the leading technology for years. However, the constant evolution of laser sources, optics and scanning systems has opened a new research field of laser cutting where quality can be further improved and processing speed further increased. In particular, the most recent literature focuses on two technologies: ultra-short, pulsed lasers to maximise cut quality and single-mode (SM) continuous wave (CW) lasers to guarantee maximum production and reduce HAZ size (when compared to multi-mode CW lasers).

Though nanosecond pulsed lasers allow for a low thermal contribution, this technology can also lead to superheating of the material surface when the pulse rate is high and result in material ablation creating a clearance width [6]. Gu *et al.*[10] investigated femtosecond laser cutting of LFP, showing that high power leads to significant decline in battery performance by creating delamination and substantial remelting in the HAZ. Zhang *et al.*[12] conducted a study on graphite anode showing that both HAZ size and delamination width increase with laser power and pulse width. The corresponding Raman analysis revealed that the ordered graphite structure is partially damaged near the kerf edge, limited to the coloured changed zone. In other words, transitioning from a primarily conduction-based process (with continuous wave lasers) to the application of ultrashort pulses leads to material removal through ablation, occurring within picosecond to femtosecond timescales. It is therefore crucial to adjust the peak fluence to ensure sufficient material removal while preventing heat dissipation into surrounding material, which could cause defects such as the heat-affected zone (HAZ) and burrs[4]. Laser source manufacturers have introduced an innovative burst mode feature, allowing control over pulse energy. Heidari *et al.*[4] found that increasing the number of pulses per burst and frequency lowers the peak fluence of each pulse, making it easier to fine-tune the optimal peak fluence and achieving higher processing speeds. Audouard *et al.*[13] applied GHz-burst mode for anode cutting and stated that the cutting time is mainly driven by the metal collector of the electrode (Cu-foil for anode, Al-foil for cathode).

Despite the notable results regarding cut quality of ultrafast lasers, the need for increased production and lower cost of laser sources of the LIBs industry has attracted attention towards SM-CW lasers as they can achieve higher processing velocities. With maximum speed of 5 m/s and maximum power of 450 W, experimental studies using SM-CW remote lasers were conducted on both anode and $LiCoO_2$ cathode[14]. A relatively wide parameter window for good cut was defined for both anode and cathode by focusing on the relationship between line energy and kerf width. For the graphite anode, a clearance width of 25 μm to 27 μm was found and determined not significant with respect to battery performance. From a computational perspective, Lee *et al.* conducted simulations of SM-CW laser on both anode and NMC cathode, showing that penetration depth and absorptivity change significantly when the laser beam reaches the metal current collectors. This is mainly due to pool flow patterns, temperature distribution, material properties and composition changes at the interfaces [2]. Lee *et al.* also conducted a study focusing on SM-CW laser cutting of compressed and uncompressed LFP cathodes up to 5 m/s, measuring absorption coefficients of graphite and copper. Because of the lower melting point and favourable gasification, the graphite undergoes a significant delamination, leading to a decrease in active material and battery capacity [15]. In other words, the different melting point between current collector and active material causes a higher heat conduction on the active material as more time is needed to cut the metal foil, leading to a grater energy transfer. To assess the more efficient laser source on cutting of current collectors, a recent study made a comparison of cut quality of Cu- and Al- foils between nanosecond pulsed lasers and SM-CW laser. The investigation revealed that the SM-CW laser obtains better cut quality, with fewer burns, less spatter and an increased quality of kerf geometry when high speeds are set [16].

This study aims to be an extension of the previous one, investigating the interaction of electrodes with high-quality, high-power CW laser source and high-speed scanning system. In fact, the current state-of-the-art lacks an investigation on the effect of SM-CW fiber laser on high-speed electrode cutting, which this paper aims to provide by applying speed up to 11 m/s and power up to 1140 W. The effect of laser parameters of a SM-CW laser was investigated on both graphite anode and LFP cathode to demonstrate the true potential of this technology by enabling rapid processing without sacrificing edge quality, obtaining fine cuts at $>$ 5 m/s and 1 kW. Correlations between irradiance and fluence are determined with respect to HAZ width for both cathode and anode, clearance width with respect to anode and quantification of spherical droplets with respect to LFP cathode.

2. Experimental set up

2.1. Materials, laser sources and cutting set-up

Commercial LFP cathode and graphite anode films were tested. A lithium-ion battery anode material made of copper foil with equal-thickness graphite layers coated on both sides was provided. The copper foil measured 8 μm in thickness, whereas each graphite layer was 66 μm. Graphite is composed of active graphite powder (90 %), carbon black (7 %), sodium carboxymethyl cellulose CMC (2 %), polymer binder (1 %). The composition of the given LFP sample was estimated through thermal-gravimetric analysis (TGA) with TA instrument TGA Q50, resulting in LFP (93.88 %), polyvinylidene fluoride PVDF + carbon black (6,12 %).

Layer thicknesses were measured with SEM-FEG microscopy (SEM, Tescan Mira3 with a Schottky emitter) by positioning the anode sample orthogonal to the plane. The Al-foil measured 14 μm and each LFP layer 80 μm. Additionally, the element composition of LFP remelted on the section was investigated by energy-dispersive X-ray spectroscopy (EDS) analysis, using a silicon drift detector (SSD). SEM accelerating voltage was set at 12 kV with a working distance of 14 mm, a current of 200/250 pA and the count rates for EDS at 3000 cps.

All the pictures were acquired with the SE (Secondary Electrons) detector, the anode samples also with the BSE detector (Backscattered electrons). BSE images show high sensitivity to differences in atomic number; the higher the atomic number, the brighter the material appears in the image. Hence, copper was bright light and graphite dark black (see Fig. 1), and it was therefore easier to quantify the clearance width with image processing in all anode samples.

An n-light Corona fiber laser source with emission wavelength of 1064 nm, maximum output power of 1.2 kW was applied for the experiments. A 2D galvo scanner system (Scanlab Intelliscan 20) was employed to move the laser beam with speed reaching up to 11 m/s. The scanner was equipped with a 163 mm focal length f-theta focusing lens achieving a 22 μm diameter spot on electrode surface. The electrode film was prepared in 3.0x3.5 mm size and held onto a vacuum chuck to remain flat and in tension without incurring defocusing issues. At the top plate of the fixture, where the electrode lies, a narrow groove was machined less than 5 mm in width. This groove allows material to escape from the cutting kerf, preventing it from reattaching at the back. The cut length was 10 mm. A clean ambient environment with constant temperature was provided for the experiments. No shielding gas was applied. The cutting was performed with suitable exhaust systems in a clean and dust-free environment.

2.2. Cutting parameters

The laser power ranges from 190 to 1140 W and the laser speed from 0.3 to 11 m/s. The different combinations of power and speed were chosen with the aim of evaluating the effect of irradiance and fluence. Irradiance I was determined as the ratio of laser power to the spot area, while fluence F was calculated as the product of Irradiance and the interaction time. The interaction time represents the duration for which the laser beam remains within a spot diameter of 22 μm (spot size) and it

Table 1
Parameters for anode and cathode continuous wave remote laser cutting (P, power; I, Irradiance and F, fluence).

	P (W)	I (MW/cm^2)	Speed (m/s)	F (J/cm^2)		P (W)	I (MW/cm^2)	Speed (m/s)	F (J/cm^2)
A1	190	50	1.83	600	D1	760	200	7.33	600
A2			1.10	1000	D2			4.40	1000
A3			0.73	1500	D3			2.93	1500
A4			0.55	2000	D4			2.20	2000
A5			0.44	2500	D5			1.76	2500
A6			0.37	3000	D6			1.47	3000
A7			0.31	3500	D7			1.26	3500
B1	380	100	3.67	600	E1	950	250	9.17	600
B2			2.20	1000	E2			5.50	1000
B3			1.47	1500	E3			3.67	1500
B4			1.10	2000	E4			2.75	2000
B5			0.88	2500	E5			2.20	2500
B6			0.73	3000	E6			1.83	3000
B7			0.63	3500	E7			1.57	3500
C1	570	150	5.50	600	F1	1140	300	11.00	600
C2			3.30	1000	F2			6.60	1000
C3			2.20	1500	F3			4.40	1500
C4			1.65	2000	F4			3.30	2000
C5			1.32	2500	F5			2.64	2500
C6			1.10	3000	F6			2.20	3000
C7			0.94	3500	F7			1.89	3500

is calculated as spot/speed. Six levels of irradiance and seven levels of fluence were chosen, with a range of 50–300 MW/cm^2 and 600–3500 J/cm^2 respectively. Detailed process parameters are summarized in Table 1.

2.3. Characterization of cut quality

Three main situations occurred for each electrode material: partial/no cut, presence of defects, good cut. To evaluate the cutting quality of each experiment, digital microscopy (DM, Keyence VHX-7000) and SEM-FEG microscopy were used. Defects were classified for each material as shown in Fig. 1. The defects considered on the anode were the HAZ width and max clearance/burr area. The defects considered on LFP cathode were the HAZ width, the quantity of spherical defects detached from the aluminum foil and the resulting diameter. Only the spherical droplets on the front side were counted.

More specifically, DM was used to provide a preliminary assessment of cut quality and measurements of HAZ width. The HAZ was measured manually as the distance from the cut edge to the color transition boundary of the unaffected area on both cathode and anode. To ensure consistency, measurements were conducted with the same lighting and imaging settings in the DM. For each sample three orthogonal measurements of the bottom-edge of each cut across each sample were taken and an average HAZ width was calculated, as shown in Fig. 1. Measuring HAZ width is crucial to minimizing thermal damage to the electrode, as excessive heating can degrade the active layer, affect electrochemical stability, and cause non-uniform current distribution, leading to increased internal resistance and reduced battery lifespan [10].

High-quality images for clearance quantification were carried out with SEM on the same surfaces for anode. One representative image was analysed for each cut. A high contrast was set (BSE channel) to identify the non-coated copper in white, as opposed to the black graphite. A MATLAB script was used to process multiple grayscale images to calculate and highlight white pixel areas. Each image was binarized using a threshold to distinguish white regions (set to 0.5) and then converted to microns based on a set scale factor. This led to an automated quantification of clearance area, which allowed for the calculation of the average clearance width.

The classification of spherical defects on cathode material was conducted based on the number of droplets on the bottom-edge of each cut, deposited on the LFP active material, as they detached from the Al-current collector, as shown in Fig. 1. The importance of such quantification method is because detached droplets (DDs) could create

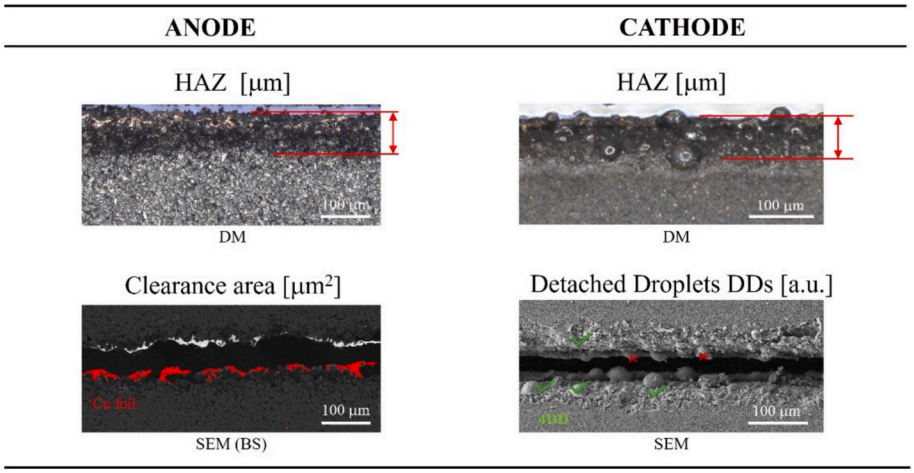

Fig. 1. Characterisation of defects created by CW laser cutting of graphite anode and LFP cathode. Digital Microscopy (DM) images show HAZ quantification for both electrodes; scanning electron microscope (SEM) images show clearance area for anode and detached droplets (DDs) for cathode.

Table 2
Classification of each cut performed with SM-CW laser cutting of graphite anode and LFP cathode. SEM images are categorised according to three classes of partial/not cut, good cut and the defect of anode and cathode, with respective parameter exposure.

Class	Partial/no cut	Good cut	Defects
Exemplary class image of anode	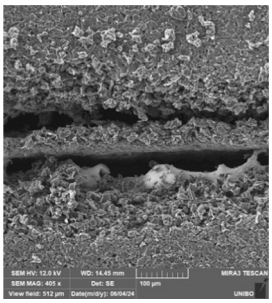	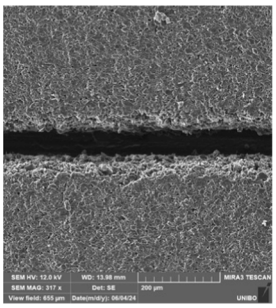	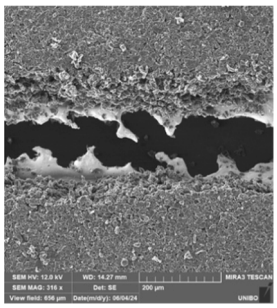
Parameters Description	A1 Full penetration is fragmented, with segment of graphite.	E3 Linear edges with full laser penetration.	A7 Presence of clearance, Cu-foil is exposed in the shape of jagged burrs.
Exemplary image of cathode	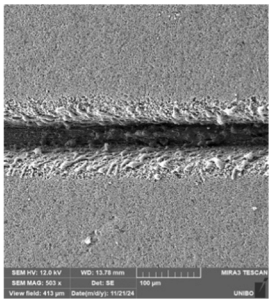	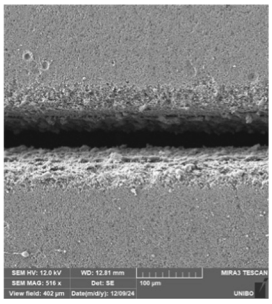	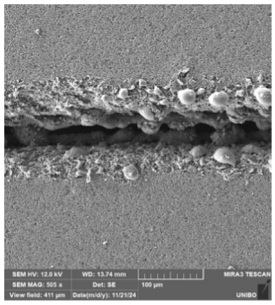
Parameters Description	D1 Only partial penetration across entire cut.	E2 Linear edges with full laser penetration.	C7 Formation of large spherical droplets, detached from Al-foil.

conductive bridges between the metal current collector and the active material, increasing the risk of internal short circuits. Additionally, oxidation and contamination of spatter may further degrade the electrochemical stability of the electrode [10,17]. The quantity of spherical defects on the cathode was calculated through four high-quality images obtained at the SEM, to assess the relevance of the formed droplets based on 3D vision and deeper understanding for droplet characterization. Some EDS analyses were also performed. To analyse the same point on each cut, each image was taken 3 mm from the beginning of the cut with x250 mag. Subsequently, three images with x500 mag were taken moving towards the opposite end of the cut. The size of DDs was taken from a single representative SEM picture of each cut. Overall, four images were acquired for each cut at the front for a total of 336 pics (considering 84 samples). Additionally, two images for the good cut and defects category were investigated at the back and at the section to assess the presence of a clearance width and DDs. Hence, 8 pics for anode and 8 pics for the cathode were added to the analysis. For a total of 352 SEM pictures.

3. Results

The images obtained from DM and SEM of each cut were divided into three categories: firstly partial/no cut, secondly good cut when edges were found smooth and absent of defects and lastly, the cuts that present a high threshold of defects, as shown in Table 2, for both anode and cathode. The following section will firstly analyse the graphite anode with respect to clearance and HAZ width, followed by the characterisation of the LFP cathode with respect to the formation of detached droplets and HAZ width.

Overall, 42 different sets of parameters were tested on each material. For preliminary considerations, Table 3 shows the quantity of performed cuts belonging to each category. It can be noted how the graphite anode exhibited 45 % more experiments that did not achieve full penetration. This is attributed to the higher melting point of Cu (1083 °C) compared to Al (661 °C) [18], along with its higher thermal conductivity, which reflects the relevance of the current collector. For the *good cut* category, four cut samples were selected for the cathode and only three for the anode, highlighting a more complex SM-CW laser cutting optimization for the latter.

3.1. Anode cutting

In this section, the cutting samples are evaluated in terms of fluence and irradiance to characterize the highest quality achievable and to analyse the influence of process parameters on the typical rising defects: HAZ and delamination width.

3.1.1. Clearance width

During laser cutting of anodes, delamination occurs at the cut edge. This phenomenon is primarily influenced by the differing thermal and optical properties of the anode's components. The copper foil, due to its lower absorptivity and higher thermal conductivity, exhibits higher ablation thresholds and lower material removal rates compared to graphite. The portion of absorbed energy exceeding the ablation threshold of copper is used for material removal, while the residual heat diffuses across the copper's surface due to its high thermal conductivity. Because of the lower ablation threshold of graphite, the residual heat can then be absorbed by graphite layers, resulting in their ablation creating clearance width. This phenomenon explanation is demonstrated by our experimental results: on the backside of good cut sample in Fig. 2 no copper foil is visible and only a small amount is observable on the front side due to direct interaction with the laser beam. No

Table 3
Total class assignment with respect to anode and cathode.

	Anode		Cathode	
	Total	Parameters	Total	Parameters
Partial/ no cut	9	A1, A2, B1, C1, D1, D2, D3, E1, F1	5	B1, C1, D1, E1, F1
Good cut	3	C4, E2, E3	4	D2, E2, E3, F2
Defects	30	A3-A7, B2-B7, C2, C3, C5-C7, D3-D7, E4-E7, F2-F7	33	A1-A7, B2-B7, C2-C7, D3-D7, E4-E7, F3-F7

degradation is caused by heat conduction, as observed instead in the "bad cut".

The *no-cut* conditions were found for each level of power at their maximum speed, which corresponds to a fluence of 600 J/cm^2. Increasing fluence up to 2000 J/cm^2 resulted in optimal cutting, with some samples exhibiting a delamination width under 25 μm. These results align with existing studies, such as Lee *et al.* [19] which demonstrate that higher speeds result in lower delamination width due to reduced energy absorption and shorter interaction times.

Minimum delamination widths of 17 μm (upper layer) and 8 μm (lower layer) were achieved at irradiance levels of 250 MW/cm^2 and fluence of 1000 J/cm^2. These values are comparable to those reported in other studies, as summarized in Table 4. Specifically, Lee *et al.* [14] have obtained the smallest clearance width of 25 μm with the highest speed of 5 m/s. This investigation therefore provides an improvement of 32 % on the clearance width with a 10 % increase in speed.

When high fluence and low irradiance (low speed and low power) are set, thermal effects exacerbate, increasing delamination width. When a threshold of F > 2000 J/cm^2 deterioration of edge consistency arises, and delamination width increases until the current collector forms *jagged burrs*, highlighted by the black bubbles at the top left in Fig. 3**a**. These observations corroborate findings from our previous study [16], which showed that when cutting bare foils with excessive energy input at low speeds causes significant melting, resulting in bubble-shaped recasts along the cut edge and poor kerf quality.

Conversely, high irradiance combined with high speeds minimized thermal diffusion but increase turbulence at the cut edge, contributing to spatter formation. This interaction causes molten copper to spatter upward, depositing onto the upper graphite layer, as evidenced by the spatter diameters ranging between 2–5 μm observed in SEM images in Fig. 2. Spatters were found exclusively in the cutting section.

Table 4
Anode Delamination width comparisons across literature.

Reference	Clearance width	Process Parameters	Set up
this paper	17 μm	950 W, 5.5 m/s	CW
[20]	40 μm	300 W, 0.25 m/s	CW
[14]	25 μm	450 W, 5 m/s	CW
[12]	27 μm	250 fs, 20 W, 0.050 m/s	PW
[5]	35 μm	10 ps, 32.4 W, 0.2 m/s, N = 10	PW-burst

3.1.2. *Heat-affected zone (HAZ)*

The size of visible color-changed zone can be easily measured by the DM. However, further examination with SEM revealed that color-changed zone is not a typical HAZ as material is not burnt, but rather crumbled. This suggests that a higher HAZ indicates partial damage to the ordered graphite structure due to excessive heat input.

HAZ size increased significantly with higher power and lower speeds. A threshold irradiance value of 150 MW/cm^2 was identified, beyond which HAZ sizes peaked, as shown in Fig. 3**d**. The lower layer consistently showed smaller HAZ sizes compared to the upper surface, likely due to reduced thermal exposure as the beam moved through the material.

The optimal process parameters for graphite anode cutting were identified within the range of I ≤ 150 MW/cm^2 and F ≤ 2000 J/cm^2. This parameter window achieved minimal defects, with delamination widths as low as 17 μm and HAZ sizes up to 30 μm. High speeds and moderate power settings were critical in minimizing thermal conduction and achieving fine cuts.

While ultrafast lasers achieve excellent quality, the results demonstrate that SM-CW lasers, when optimized, offer a cost-effective alternative with comparable quality at significantly higher processing speeds. Adjustments in beam focus and speed can mitigate spatter formation, particularly in multi-layer configurations where molten material interacts with adjacent layers.

3.2. *Cathode cutting*

This section analyses the cut samples of LFP cathode to determine the highest cut quality. This is achieved by characterising detached spherical droplets (DDs) and HAZ width in correlation with irradiance and fluence.

3.2.1. *Spherical defects*

The laser interaction with LFP cathode leads to the formation of spherical droplets on both the current collector and the active material

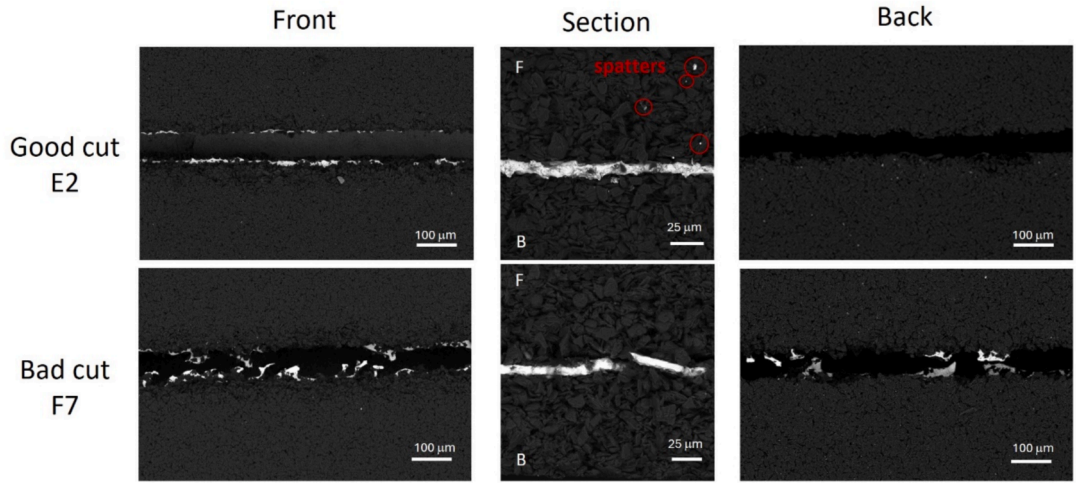

Fig. 2. Top, section and back SEM images of anode cut samples following exposure at 950 W – 5.5 m/s (Good cut) and 1140 W – 1.9 m/s (Bad cut). Spatters can be noticed in the upper layer of graphite (front F) in the good cut conditions.

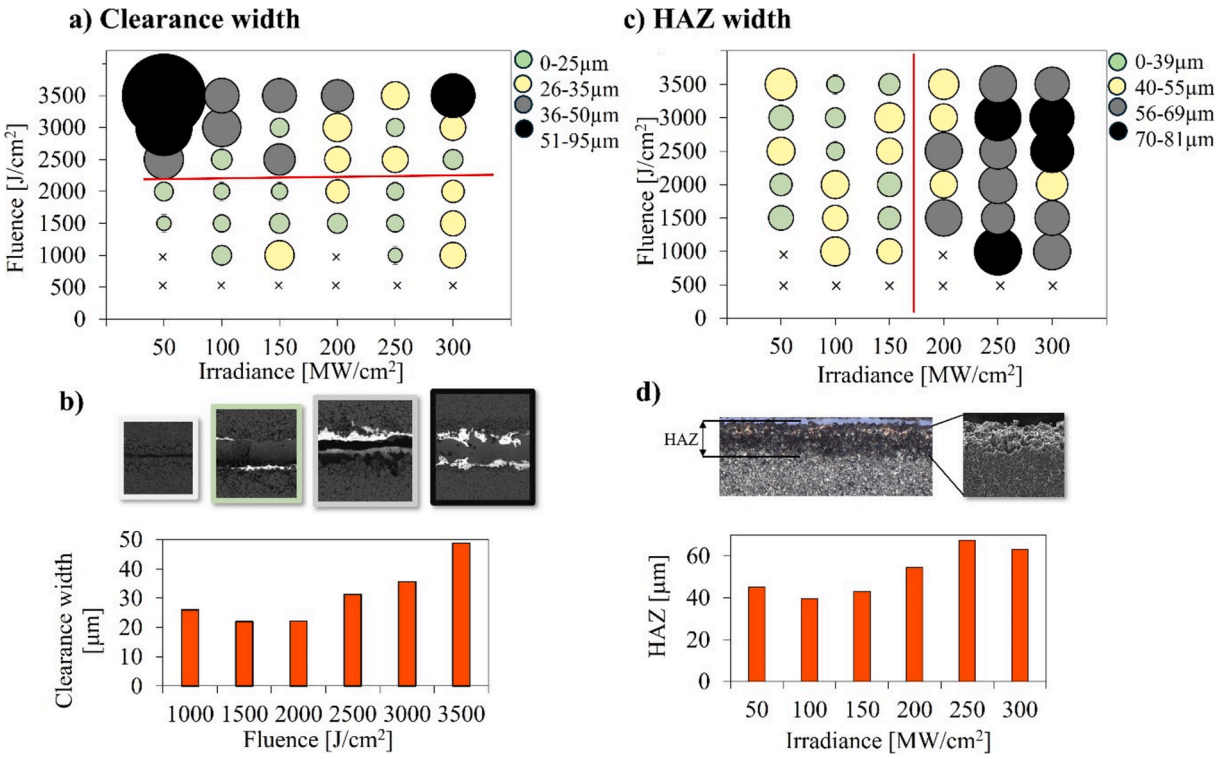

Fig. 3. a) Bubble graph of clearance width for anode cut samples. b) Correlation of clearance width with fluence. c) Bubble graph of HAZ width for anode cut samples d) Correlation of average HAZ width with irradiance.

coating. These droplets are hypothesized to follow a similar mechanism of formation to that of spatters, previously characterised by Angeloni *et al.* [16], with the significant difference of creating sphere shaped droplets of remelted material, detached from the current collectors. Such detached droplets (DDs) decrease cut quality and battery performance. The formation is attributed to the thermal conduction of heat across the electrode material. Specifically, by analysing the front, section and back of samples shown in Fig. 4, it is evident that heat is the main cause of DDs formation. In fact, it can be observed that the front-side of the cut presents a higher number of DDs compared to the back side. This is further confirmed by the section profiles shown in Fig. 4, where spatter formation leading to DDs is mostly present on the cathode interface that directly interacts with the laser source.

Though LFP is the most stable cathode material commercially used in LIBs production, the reaction with Al-current collector at very high temperatures and pressure, leads to the evaporation of some material, while a portion undergoes remelting in the shape of droplets. Energy dispersive spectroscopy (EDS) analyses were performed on the section profiles of cut samples, reported in Fig. 5, to qualitatively assess the composition of the remelted material in comparison to unaffected active material. Specifically, the SEM section view in Fig. 5a shows that the affected material exhibits lower carbon percentage and higher percentages of phosphorous and iron. This agrees with Raman analyses conducted by Lutey *et al.* [21], where they compared the structural changes on unaffected LFP with affected LFP in the form of spherical defects. Results showed a reduction or complete absence of carbon bands in the remelted spherical defects as well as a sharpening of the olivine peak (crystal structure of LFP). The affected material is therefore subject to remelting with fast recrystallisation, leading to lattice structure and composition changes in the remelt. EDS analyses also show that the remelted material is significant to the point of resolidifying over the cut portion of Al-foil, forming an inhomogeneous LFP layer, as shown in Fig. 5b where 88 % aluminium was detected across one of the cracks present in the remelt layer. In fact, it is hypothesized the remelted material over the Al-foil is prone to cracking because of fast recrystallisation, high cooling speed and very low thickness. These cracks can result

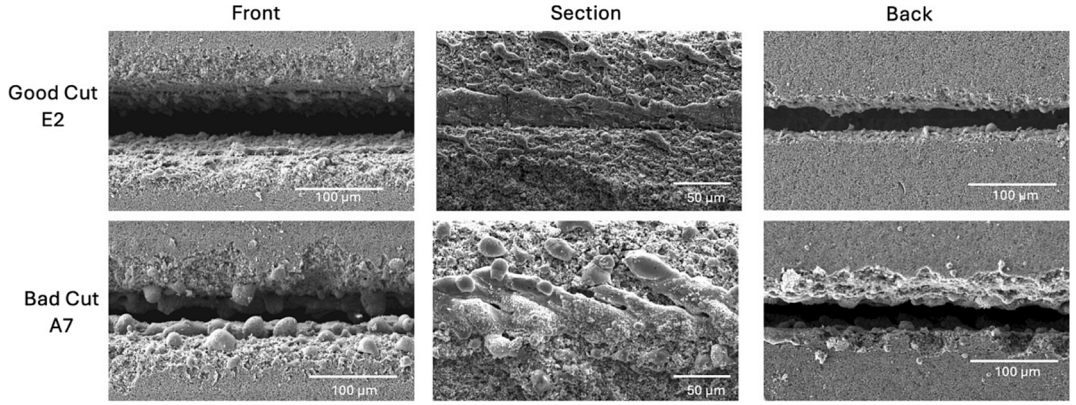

Fig. 4. Front, section and back SEM images of cathode cut samples, following exposure at 950 W- 5.50 m/s (good cut) and 190 W-0.31 m/s (bad cut).

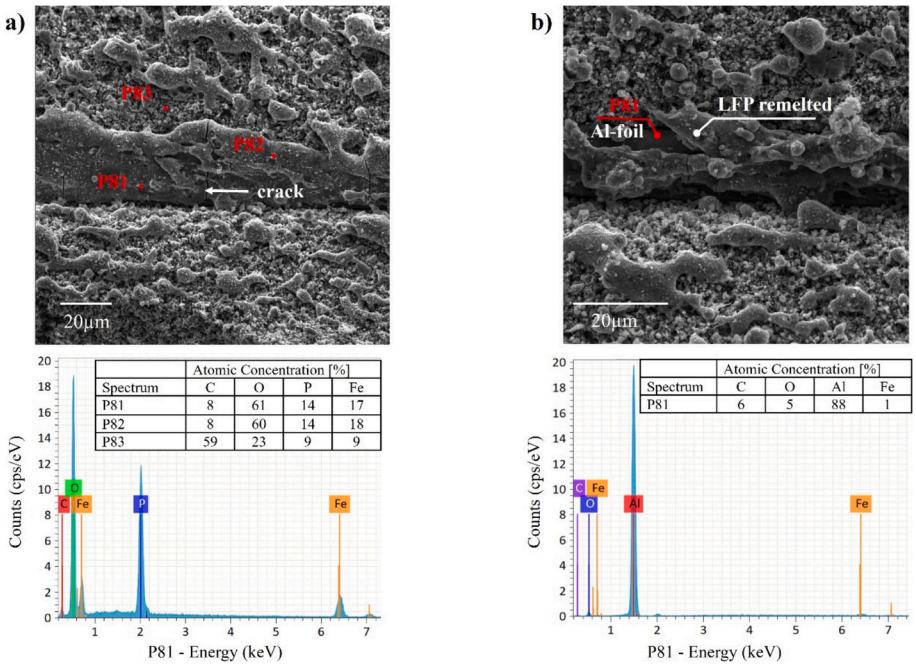

Fig. 5. EDS analysis of section profile of cut sample A7 showing a) remelted LFP layer and b) Al-foil underneath remelted active material.

in detachment of remelt-LFP leading to short circuits as well as decreased conductivity upon activation of the battery cell.

The numerical estimation of DDs created by SM-CW laser cutting on LFP cathode is shown in Fig. 6**a** where each colour represents a quantity in arbitrary units. DDs are counted from SEM images at x250 mag. The × symbol represents experiments classified as partial/no cut. In fact, the optimal cuts with one or no DDs were found between 1000 and 2000 J/cm^2, attributed to the lower energy transfer to both the active material and Al-foil, which limits the melting and subsequent solidification of the material. Specifically, *good cut* quality was found with parameters B2-B4, C1-C2, C4, D2, E2-E3, F2-F4 (Fig. 6**a**).

Being the first in the literature with a numerical estimation of spherical defects, no direct comparison with other laser sources is possible. However, the analysis reveals that the higher the fluence, the higher number of DDs are formed with a larger diameter on average, as shown in Fig. 6**b**. Specifically, minimum diameter sizes (in the range of 10.7 µm–16.4 µm) were found for high irradiances ranging between 200 to 300 MW/cm^2 and low fluences of 1000 to 1500 J/cm^2, with a minimum diameter of 10.7 µm for sample E2 (I = 250 MW/cm^2 and F = 1000 J/cm^2). This is in accordance with Baumann *et al.* study [22] who evaluated that higher scan velocities result in lower quantity of spatter. Conversely, the higher values of particle diameters (in the range of 27.9 µm – 35.1 µm) are found at low irradiances of 50–150 MW/cm^2 and high fluences of 3000 to 3500 J/cm^2, peaking at 35.1 µm for sample A7 (I =

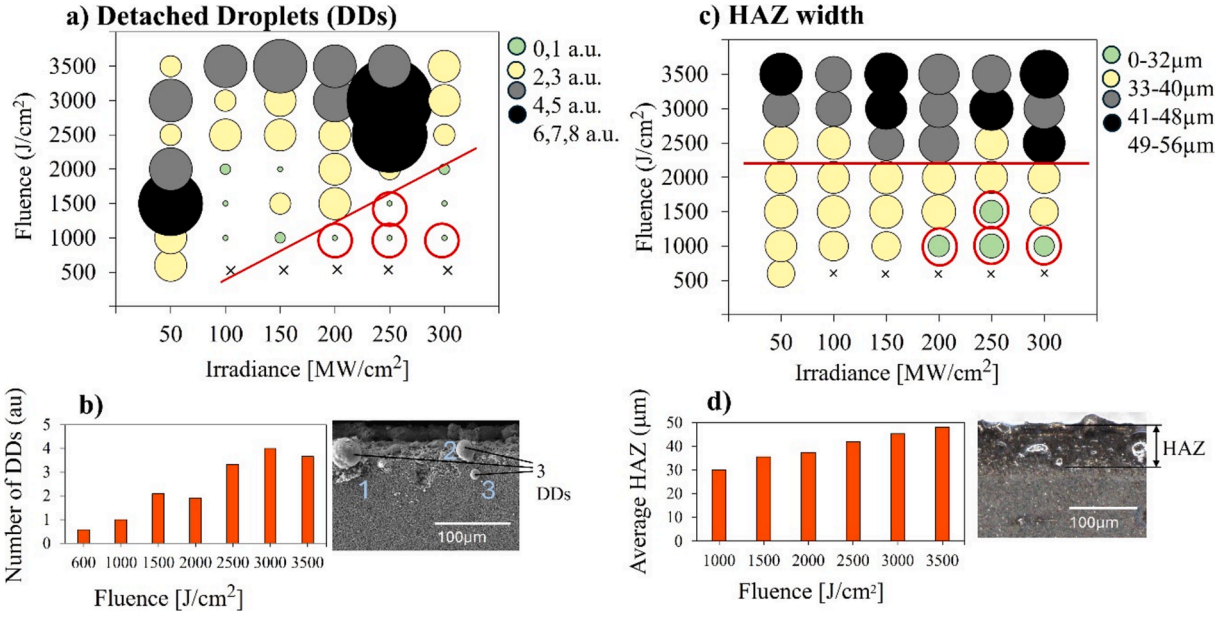

Fig. 6. a) Bubble graph of DDs for cathode cut samples. b) Correlation of DDs with fluence. c) Bubble graph of HAZ width for cathode cut samples d) Correlation of average HAZ width with fluence.

50 MW/cm^2 and F = 3500 J /cm^2). Therefore, the quantification of DDs revealed a direct relationship between number and size of DDs, where the formation of more DDs is associated with a larger diameter and vice versa.

3.2.2. Heat affected zone (HAZ)

The colour-changed zone or HAZ was easily measured from DM images. Thanks to SEM analysis, a similar crumbling phenomenon to that of the anode was also observed on cathode active material. The effect of irradiance and fluence on HAZ width on LFP cathode is shown in Fig. 6**c**, where each colour represents a width range of HAZ. The "×" symbol represents experiments classified as partial/no cut.

It can be observed from Fig. 6**d** that thermal degradation increases with fluence. The HAZ measurements in Fig. 6**c** confirm that interaction time is the dominant factor in quality deterioration, as the HAZ becomes excessively large for all irradiance levels at Fluences $\geq$ 2500 J/cm^{-2}. These results suggest that while irradiance variations showed negligible impact on HAZ growth, the process achieves optimal results at higher speeds, where shorter interaction times mitigate thermal damage.

The analysis showed that HAZ sizes are of medium size with respect to fluence up to 2000 J/cm, to then reach a *threshold* and exhibit a width of more than 40 μm width. The minimum HAZ width was 24 μm and it was achieved for irradiance level of 300 MW/cm^2 and fluence of 1000 J/cm^2. The optimal parameter window with respect to HAZ width is determined to be between 4.40 m/s at 760 W, 3.67–5.50 m/s at 950 W and 6.60 m/s at 1140 W, as highlighted by the red circles in Fig. 6**c**. Existing literature on LFP cathode found good quality at 250 W, 3.5–5 m/s with SM-CW laser [14]. In this study, good cut quality was determined for high speeds and power, with maximum speed of 6.60 m/s and 1140 W, with minimised defects including spherical defects and HAZ. Therefore, the use of SM-CW laser proves to be efficient at high speeds and power for LFP cutting, leading to an optimised production.

4. Conclusions

The analysis conducted in this study has proved significant quality enhancement when high-quality continuous wave laser beams are applied to cut commercial electrodes. For the graphite anodes, a minimum clearance width of 17 μm was found at 950 W and 5.5 m/s, significantly improving the current state-of-art by minimizing heat affected zones and material evaporation providing a 32 % improvement on the clearance width with a 10 % increase in speed. HAZ width on the graphite anode exhibited a strong relationship with irradiance, increasing with higher power and lower speeds due to greater heat accumulation. On the other hand, cathode HAZ width exhibited a linear correlation with fluence, with lower speeds causing more material crumbling. An experimental systematic method was successfully presented to estimate spherical droplet formation (DDs) on the cathode. The analysis of spherical droplets (DDs) detached from the current collector led to a new insight with respect to laser speed: DDs formation is promoted by low velocities and low power. Therefore, optimal cutting of the LFP cathode was achieved at high power and speeds above 5 m/s, with a maximum speed of 6.6 m/s representing a 32 % increase in processing efficiency compared to the current state-of-the-art, enabled by increased beam quality and higher power.

CRediT authorship contribution statement

Caterina Angeloni: Writing – original draft, Investigation, Data curation. **Carolina Magrini:** Writing – original draft, Investigation, Data curation. **Erica Liverani:** Writing – review & editing, Methodology, Data curation, Conceptualization. **Alessandro Fortunato:** Supervision, Resources.

Declaration of competing interest

The authors declare that they have no known competing financial interests or personal relationships that could have appeared to influence the work reported in this paper.

Acknowledgments

This research did not receive any specific grant from funding agencies in the public, commercial, or non-profit sectors.

Data availability

Data will be made available on request.

References

[1] M.G. Berhe, H.G. Oh, S.-K. Park, D. Lee, Laser cutting of silicon anode for lithium-ion batteries, J. Mater. Res. Technol. 16 (2022) 322–334, https://doi.org/10.1016/j.jmrt.2021.11.135.
[2] D. Lee, R. Patwa, H. Herfurth, J. Mazumder, Computational and experimental studies of laser cutting of the current collectors for lithium-ion batteries, J. Power Sources 210 (2012) 327–338, https://doi.org/10.1016/j.jpowsour.2012.03.030.
[3] J. Suk, D.Y. Kim, D.W. Kim, Y. Kang, Electrodeposited 3D porous silicon/copper films with excellent stability and high rate performance for lithium-ion batteries, J. Mater. Chem. A 2 (2014) 2478, https://doi.org/10.1039/c3ta14645f.
[4] P. Heidari Orojloo, A.G. Demir, Study of burst mode for enhancing the ps-laser cutting performance of lithium-ion battery electrodes, J. Laser Appl. 36 (2024) 042013, https://doi.org/10.2351/7.0001417.
[5] A.H.A. Lutey, A. Fortunato, S. Carmignato, M. Fiorini, High speed pulsed laser cutting of LiCoO 2 Li-ion battery electrodes, Opt. Laser Technol. 94 (2017) 90–96, https://doi.org/10.1016/j.optlastec.2017.03.022.
[6] A.H.A. Lutey, A. Fortunato, A. Ascari, S. Carmignato, C. Leone, Laser cutting of lithium iron phosphate battery electrodes: Characterization of process efficiency and quality, Opt. Laser Technol. 65 (2015) 164–174, https://doi.org/10.1016/j.optlastec.2014.07.023.
[7] M. Luetke, V. Franke, A. Techel, T. Himmer, U. Klotzbach, A. Wetzig, E. Beyer, A Comparative Study on Cutting Electrodes for Batteries with Lasers, Phys. Procedia 12 (2011) 286–291, https://doi.org/10.1016/j.phpro.2011.03.135.
[8] M.R. Kronthaler, F. Schloegl, J. Kurfer, R. Wiedenmann, M.F. Zaeh, G. Reinhart, Laser Cutting in the Production of Lithium Ion Cells, Phys. Procedia 39 (2012) 213–224, https://doi.org/10.1016/j.phpro.2012.10.032.
[9] J. Kriegler, T.M. Duy Nguyen, L. Tomcic, L. Hille, S. Grabmann, E.I. Jaimez-Farnham, M.F. Zaeh, Processing of lithium metal for the production of post-lithium-ion batteries using a pulsed nanosecond fiber laser, Results Mater. 15 (2022) 100305, https://doi.org/10.1016/j.rinma.2022.100305.
[10] X. Gu, X. Sun, Y. Han, Q. Li, J. Liu, X. Mei, Femtosecond laser cutting of LiFePO4 electrodes: Kerf geometry, process optimization, and electrochemical performance, J. Storage Mater. 101 (2024) 113859, https://doi.org/10.1016/j.est.2024.113859.
[11] T. Jansen, M.W. Kandula, D. Blass, S. Hartwig, W. Haselrieder, K. Dilger, Evaluation of the Separation Process for the Production of Electrode Sheets, Energ. Technol. 8 (2020) 1900519, https://doi.org/10.1002/ente.201900519.
[12] Y. Zhang, J. Li, R. Yang, T. Liu, Y. Yan, Analysis of kerf quality on ultrafast laser cutting of anode material for lithium-ion battery, Opt. Lasers Eng. 118 (2019) 14–21, https://doi.org/10.1016/j.optlaseng.2019.01.013.
[13] E. Audouarda, D. Pallarèsb, J.-M. Romanob, F. Mermet, M. Fleureaua, Characterization of batteries materials ablation by femtosecond pulses, (n.d.).
[14] D. Lee, R. Patwa, H. Herfurth, J. Mazumder, Parameter optimization for high speed remote laser cutting of electrodes for lithium-ion batteries, J. Laser Appl. 28 (2016) 022006, https://doi.org/10.2351/1.4942044.
[15] D. Lee, B. Oh, J. Suk, The Effect of Compactness on Laser Cutting of Cathode for Lithium-Ion Batteries Using Continuous Fiber Laser, Appl. Sci. 9 (2019) 205, https://doi.org/10.3390/app9010205.
[16] C. Angeloni, E. Liverani, A. Ascari, A. Fortunato, Characterization and process optimization of remote laser cutting of current collectors for battery electrode production, J. Mater. Process. Technol. 324 (2024) 118266, https://doi.org/10.1016/j.jmatprotec.2023.118266.
[17] T. Jansen, M. Kandula, S. Hartwig, L. Hoffmann, W. Haselrieder, K. Dilger, Influence of Laser-Generated Cutting Edges on the Electrical Performance of Large Lithium-Ion Pouch Cells, Batteries 5 (2019) 73, https://doi.org/10.3390/batteries5040073.
[18] C. Zhou, L. Jiang, Z. Gu, C. Wang, L. He, L. Huang, Z. Li, K. Li, Flexible core–shell structured Al-Cu alloy phase change materials for heat management, Chem. Eng. J. 471 (2023) 144610, https://doi.org/10.1016/j.cej.2023.144610.
[19] D. Lee, Investigation of Physical Phenomena and Cutting Efficiency for Laser Cutting on Anode for Li-Ion Batteries, Appl. Sci. 8 (2018) 266, https://doi.org/10.3390/app8020266.

[20] J. Kriegler, M. Binzer, M.F. Zaeh, Process strategies for laser cutting of electrodes in lithium-ion battery production, J. Laser Appl. 33 (2021) 012006, https://doi.org/10.2351/7.0000335.
[21] A.H.A. Lutey, M. Fiorini, A. Fortunato, A. Ascari, Chemical and microstructural transformations in lithium iron phosphate battery electrodes following pulsed laser exposure, Appl. Surf. Sci. 322 (2014) 85–94, https://doi.org/10.1016/j.apsusc.2014.10.069.
[22] R. Baumann, A.F. Lasagni, P. Herwig, A. Wetzig, C. Leyens, E. Beyer, Efficient separation of battery materials using remote laser cutting–high output performance, contour flexibility, and cutting edge quality, J. Laser Appl. 31 (2019) 022210, https://doi.org/10.2351/1.5096127.